analytical chemistry

pubs.acs.org/ac

Article

Plasmonic Biosensor Augmented by a Genetic Algorithm for Ultra-Rapid, Label-Free, and Multi-Functional Detection of COVID-19

Dongxiao Li, Hong Zhou, Xindan Hui, Xianming He,* and Xiaojing Mu*

Cite This: *Anal. Chem.* 2021, 93, 9437−9444

Read Online

ACCESS | Metrics & More | Article Recommendations | Supporting Information

ABSTRACT: The novel coronavirus (COVID-19) is spreading globally due to its super contagiousness, and the pandemic caused by it has caused serious damage to the health and social economy of all countries in the world. However, conventional diagnostic methods are not conducive to large-scale screening and early identification of infected persons due to their long detection time. Therefore, there is an urgent need to develop a new COVID-19 test method that can deliver results in real time and on-site. In this work, we develop a fast, ultra-sensitive, and multi-functional plasmonic biosensor based on surface-enhanced infrared absorption for COVID-19 on-site diagnosis. The genetic algorithm intelligent program is utilized to automatically design and quickly optimize the sensing device to enhance the sensing performance. As a result, the quantitative detection of COVID-19 with an ultra-high sensitivity (1.66%/nm), a wide detection range, and a diverse measurement environment (gas/liquid) is achieved. In addition, the unique infrared fingerprint recognition characteristics of the sensor also make it an ideal choice for mutant virus screening. This work can not only provide a powerful diagnostic tool for the ultra-rapid, label-free, and multi-functional detection of COVID-19 but also help gain new insights into the field of label-free and ultrasensitive biosensing.

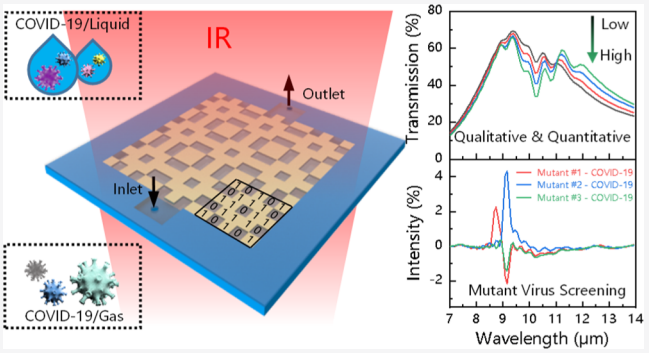

INTRODUCTION

Severe acute respiratory syndrome coronavirus 2 (SARS-COV-2, known as COVID-19) is spreading rapidly worldwide due to its extremely high contagiousness, which has had a huge impact on the global medical health system and the world economy.[1] COVID-19 is a new type of β-coronavirus, consisting of a single-stranded positive-sense RNA genome and four structural proteins [spike surface glycoprotein (S), small envelope protein (E), matrix protein (M), and nucleocapsid protein (N)].[2] The mechanism of the new coronavirus infection is through the interaction of the spike protein with the angiotensin-converting enzyme 2 receptor, thereby entering the cell and causing pneumonia.[3] As of March 1, 2021, the cumulative number of confirmed cases of COVID-19 worldwide has reached more than 114,635,654, resulting in 2,539,427 deaths.[4] Although a vaccine against COVID-19 has been developed,[5] the full vaccination of people and the effective control of the epidemic still need a long time due to the vaccine production capacity.[6,7] In addition, mutated novel coronaviruses with higher infectiousness have been discovered in the United Kingdom, South Africa, Brazil, and other places, which may make the global epidemic prevention and situation control more severe.[8] So far, precise identification of infected persons and determination of risk areas are still effective measures for timely control of the epidemic.[9,10] Through analysis of the epidemiological characteristics of infected persons and intelligent isolation of risk areas, the impact of the epidemic on the national economy can be minimized and more resources can be allocated to combat the disease more strategically.[11] Therefore, extensive, timely, and accurate identification of new viruses is essential to contain the spread of COVID-19 and control the emerging pandemic.

Currently, the commonly used diagnostic test methods for COVID-19 are mainly divided into three types: (1) reverse transcription-polymerase chain reaction (RT-PCR) test, (2) serological test or immunoassay, and (3) chest computed tomography (CT). The chest CT scan is a reliable method for diagnosing the novel coronavirus,[12,13] but a large-scale CT scan is not a practical solution. A significant limitation is that the CT scanner needs to be fully disinfected between different patients (the time for thorough disinfection may be as long as tens of minutes) to avoid new infections caused by the virus remaining on the CT scanner. Serological testing/immunoassay is an important basis for the diagnosis of confirmed and

Received: March 11, 2021
Accepted: June 15, 2021
Published: June 25, 2021

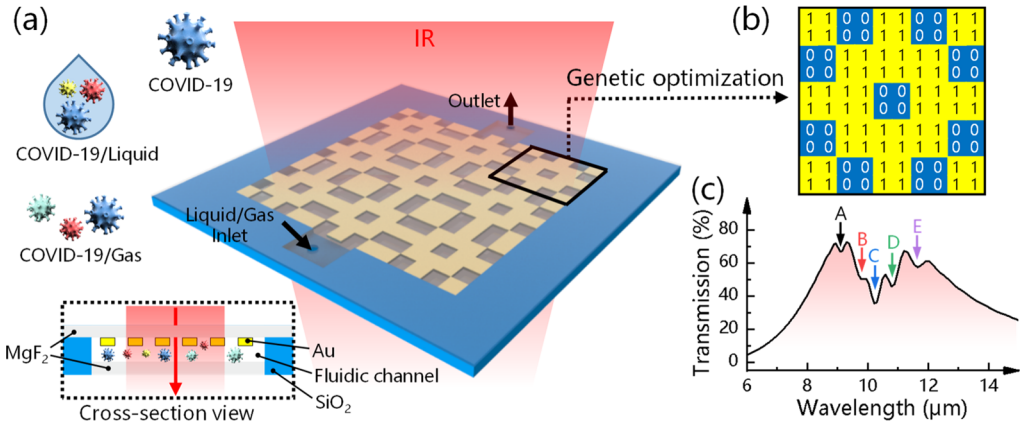

Figure 1. Plasmonic biosensors for detecting and identifying COVID-19. (a) Device configuration and sensing mechanism of the 3D plasmonic sensor. (b) GA program is used to optimize the metal structure, where "1" means nano-metal and "0" means no nano-metal. (c) Resonance position of the metal structure is designed to overlap the fingerprint vibration signals of the virus molecule, allowing simultaneous enhancement and detection of COVID-19-induced absorption changes.

suspected cases.[14,15] It detects the presence and content of specific antibodies in blood samples to indirectly determine the presence or absence of viruses in the body and the degree of virus infection. Although serological testing/immunoassay has high specificity and sensitivity, it cannot achieve the purpose of early diagnosis because virus-specific antibodies usually appear 7−14 days after the onset of disease.[16,17] Given the virus's super contagious nature, this waiting time is unreasonable in large-scale diagnosis and early screening of infected persons. Compared with antibody serological testing, nucleic acid testing can detect patients in the window period and detect infections early.[18,19] It is the current "gold standard" for novel coronavirus testing. However, the RT-PCR detection process is usually time-consuming (>3 h) and complicated. In addition, there are often false-negative results in nucleic acid testing, so many patients cannot get timely isolation and treatment before waiting for the RT-PCR test result or diagnosis, which has led to wider community transmission.[20,21] Therefore, developing a test method for real-time detection and on-site delivery of test results is necessary for large-scale early COVID-19 screening.

Fortunately, label-free biosensors provide a reliable solution for the clinical diagnosis and rapid detection of COVID-19.[22−24] Among the many biosensing technologies available, plasmonic biosensors with surface-enhanced infrared absorption (SEIRA) can be used as an excellent candidate for label-free and real-time detection of trace analytes.[25−27] The plasmonic biosensor is arranged with a layer of manually designed nano-antennas on the device's surface. These nano-antennas stimulate the plasmonic field to be enhanced under the irradiation of infrared light. The enhancement of the plasmonic field makes the nano-antenna extremely sensitive to the dielectric constant (or refractive index) of the combination near the antenna. In addition, infrared plasmonic biosensors can distinguish different analytes through spectral fingerprint vibration, which helps to directly detect and distinguish mutated virus molecules.[28] Therefore, infrared plasmonic biosensors are excellent candidates for real-time, label-free detection of trace analytes. Recently, many plasmonic biosensors have been reported, and they are widely used to detect chemical and biological molecules, such as gases,[29,30] nucleic acids,[31] and proteins.[32] The various sensing applications of infrared plasmonic sensors have brought new inspiration for virus detection. The inspiration is that the sensor can not only detect virus molecules in nasopharyngeal swabs or saliva but also directly detect virus molecules in exhaled air and droplets. Among them, the use of exhaled gas-detection methods greatly reduces the difficulty of sample collection. Therefore, for COVID-19 detection, infrared plasmonic sensors may provide a novel and attractive solution for real-time, label-free, and multi-functional virus detection.

Although infrared plasmonic sensors have proven to be a very effective solution for trace analyte detection, their detection capabilities have not yet been fully developed. The detection capability of the infrared plasmonic sensor largely depends on the structural design of the nano-antenna. In previous work, most nano-antenna designs came from manual tuning by engineers. However, manual tuning methods are often suitable for simple geometric figures, such as nano-squares, nano-discs, nano-rods, and nano-crosses. In addition, to find a nano-antenna with excellent detection capabilities, manual tuning often consumes a lot of time and wastes resources. Therefore, to obtain a plasmonic sensor with higher detection capability, it is necessary to use computer algorithms to help search and optimize the structural design of the nano-antenna.[33,34] Herein, we develop a real-time, highly sensitive, and multi-functional virus sensor by combining the genetic algorithm (GA) and finite difference time domain software (FDTD). The plasmonic sensor can not only detect the novel coronavirus in nasopharyngeal swabs/saliva but also directly detect virus molecules in exhaled air or droplets. In addition, the plasmonic sensor also has the functions of quantitative detection of COVID-19 and identification of mutant viruses. Overall, this sensing method is expected to serve as a new virus pre-screening tool to allow early detection of infected persons and the greatest control of new pandemics.

METHOD SECTION

Plasmon Biosensor for COVID-19 Detection. The plasmonic biosensing device and its sensing mechanism are shown in Figure 1. The customized metal nanostructure is deposited on the infrared-transmitting magnesium fluoride (MgF_2) substrate (n = 1.38) and forms a nanofluidic channel having a thickness of 500 nm with MgF_2 at the bottom. The nanochannel allows the flow of gas or liquid containing the sample under test. The infrared light is emitted by the light source and passes through the top MgF_2, the metal

https://doi.org/10.1021/acs.analchem.1c01078
Anal. Chem. 2021, 93, 9437−9444

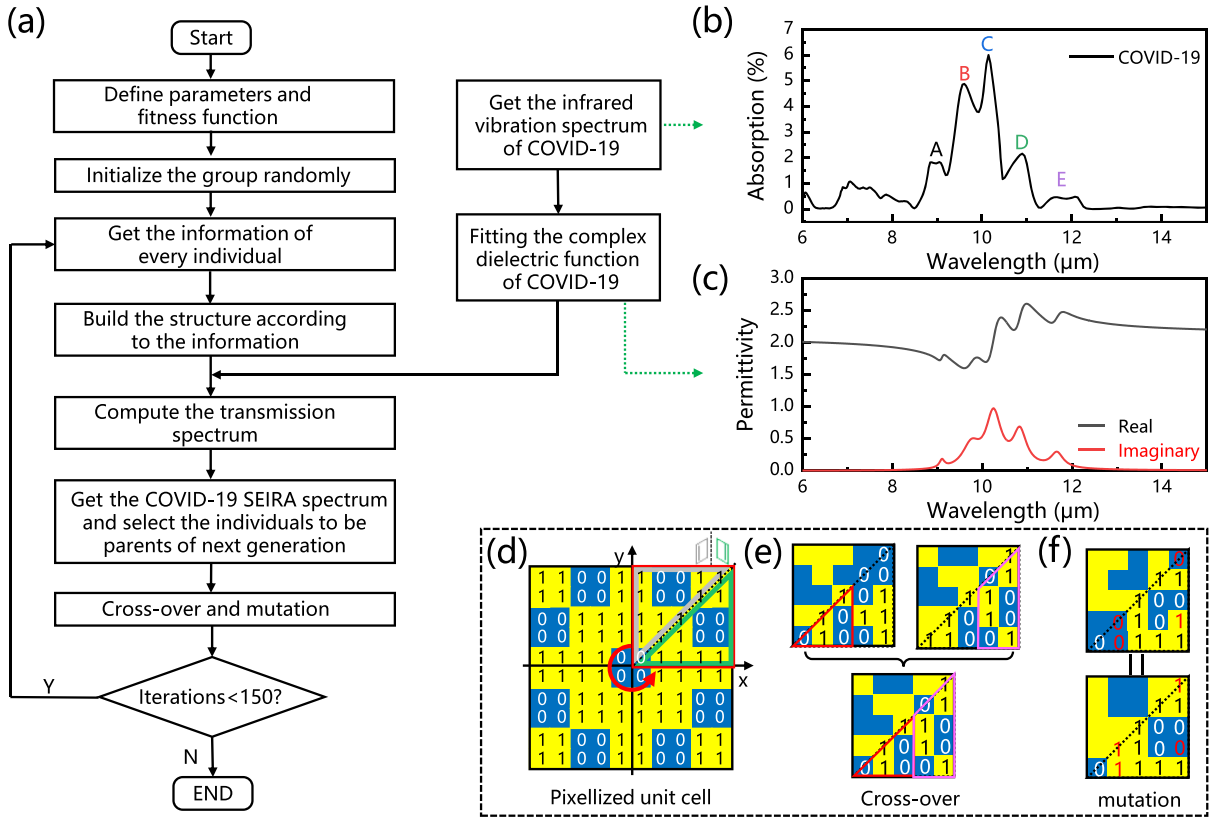

Figure 2. (a) Flow chart of the GA program used to optimize the nano-metal structure. (b) Typical infrared vibration spectrum (A–E) of γ-irradiation-inactivated COVID-19 virus particles. Reproduced from Valério, G. B.; Maneesh, N. S.; Leonardo Leal, B.; Wena Dantas, M.; Paula Frizera, V.; Jose Geraldo, M.; Rodrigo, R.-R.; Luciene, C. G. C.; Patrick, H. W.; and Francis, L. M. *Anal. Chem.* **2021**, 93, 2950−2958 (ref 11). Copyright 2021 American Chemical Society. (c) Real (black curve) and imaginary (red curve) parts of the COVID-19 molecular complex permittivity function model. (d) Geometric shape of the unit cell is pixelated into a 10 × 10 symmetrical grid, where the green region and the gray region meet the mirror symmetry rule, and the entire structure is center-symmetric. (e,f) Schematic diagrams of cross-over operation and mutation operation in the GA program, respectively.

nanostructure, the nanofluidic channel, and the bottom MgF_2 in sequence. Finally, the infrared light is collected by the infrared detector and passed to a computer for further analysis (Figure 1a). Metal nanostructures excite plasmon resonance under the irradiation of infrared light and generate local field enhancement. This local field enhancement can produce penetration depths greater than 100 nm in free space. When COVID-19 molecules are distributed on the surface of the metal nanostructure, the molecular vibration does not strongly interact with the incident light but it can be coupled with the plasmon resonator. This coupling will change the transmission spectrum line type (Figure 1c), showing the SEIRA effect. Compared with traditional infrared detection devices without metal nanostructures, the local field enhancement and penetration depth generated by metal nanostructures can effectively break through the limitations of the Beer−Lambert law and provide the possibility of detecting trace analytes. In addition, using the fingerprint vibration characteristics of the infrared spectrum, we can extract the fingerprint vibration peaks of COVID-19, which provides the possibility to identify COVID-19 molecules without marking. Simultaneously, by analyzing the intensity and linearity of the COVID-19 fingerprint vibration peak, the quantitative detection of viruses and the identification of mutant viruses can be further realized. Overall, the advantages of the infrared plasmonic biosensors are expected to provide a novel and effective way to realize large-scale and multi-functional COVID-19 detection.

The degree of overlap between plasmon resonance and molecular vibration and the local field enhancement are the keys to the device sensitivity. The above two factors are closely related to the design of metal nanostructures. In the previous work, peers often obtained a more sensitive structural design through manual adjustment. However, this manual tuning method will become very weak in the design of complex structures. In addition, in the preliminary design of the device, the manual optimization method of the metal structure will also consume a lot of time, which is unreasonable for the early development of virus-detection devices. It is necessary to use computer algorithms to quickly search and optimize the structural design with ultra-high sensitivity to solve this problem. To this end, we have developed a GA-based computer program to swiftly find nano-metal structures with ultra-high sensitivity suitable for COVID-19 detection (Figure 1b). The details are shown in Figure 2. Numerical calculation results show that through the intelligent screening of computer programs, we can obtain the ultra-high-sensitive structural design in a relatively short time, which is very beneficial for the rapid development of virus-sensing platforms.

GA Optimizing Method. The flow chart of using the GA program to optimize the nano-metal structure in a unit cell is shown in Figure 2a. The geometry of each unit cell is pixelated into a 10 × 10 symmetrical grid (Figure 2d), where "1" means nano-metal and "0" means no nano-metal. The green region in Figure 2d is the initial structure generated by the program each

https://doi.org/10.1021/acs.analchem.1c01078
Anal. Chem. 2021, 93, 9437−9444

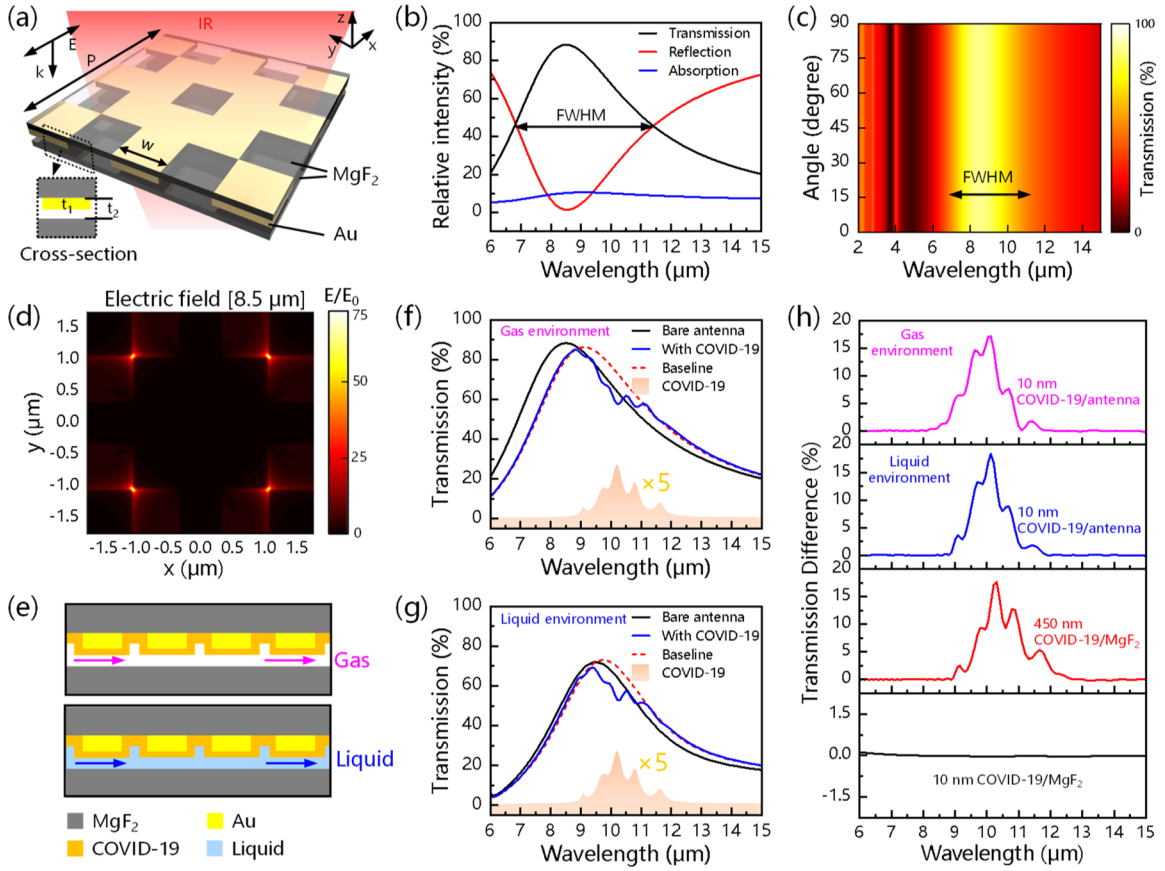

Figure 3. Optical properties and SEIRA capabilities of the proposed metal structure. (a) Schematic diagram of the transmissive plasmonic biosensor. (b) Simulated transmission (black), reflection (red), and absorption (blue) spectra of the metal structure. (c) Simulated transmission spectra of the metal structure with different polarizations. (d) Simulated electric field distribution of the metal structure at 8.5 μm. (e) Schematic diagram of plasmonic biosensor sensing in gas and liquid environments, respectively. (f,g) Simulated signal response of the analyte coated on the metal structure in a gas and liquid environment, respectively. For reference, a scaled (×5) COVID-19 absorbance spectrum is displayed as the orange-shaded region. (h) Relative signal spectra of the 10 nm COVID-19 molecular layer coated on the metal structure (magenta: gas environment and blue: liquid environment) and coated on a 400 nm MgF_2 substrate (black). The red curve in (h) refers to the relative signal spectrum of a 450 nm COVID-19 molecular layer coated on a 400 nm MgF_2 substrate.

time and the gray region and the green region meet the mirror symmetry rule. Consider the above two regions (green region and gray region) as a whole (red box) and rotate 90, 180, and 270° counterclockwise, and finally, a center-symmetric metal structure is achieved. This centrally symmetrical structural design has a polarization-independent spectral response. In addition, it can be easily extended to other symmetrical structures by modifying the program (Figure S1). Before starting the optimization procedure, we need to define the basic design parameters (such as the period of the unit cell, the thickness of the metal structure, the thickness of the microchannel, the thickness of the analyte, etc.) and the fitness function. Herein, the fitness function ($I_{COVID-19}$) is defined as the integrated value of the analyte's SEIRA signal in the 6−15 μm frequency band. After running the program, the GA program will randomly generate 20 initial populations and pass them to a FDTD simulator to generate the metal structure's original pattern. Then, the FDTD simulator will spontaneously calculate the transmission spectra of these metal structures with or without analytes and obtain the SEIRA spectra of the analytes; the specific method is shown in Figure 3. Next, the GA program selects high-quality individuals from 20 groups, eliminates inferior individuals and continuously optimizes high-quality individuals through mutation operators or cross-over operators, and finally iterates to perfect individuals. The "high-quality individual" here refers to the individual with higher $I_{COVID-19}$, and the "perfect individual" refers to the individual with the highest $I_{COVID-19}$. Figure 2e,f are schematic diagrams of cross-over operation and mutation operation, respectively (the corresponding spectral simulations are shown in Figures S2 and S3). Here, the cross-over operation refers to selecting two high-quality individuals as parents and replacing and reorganizing parts of their structures to generate new individuals. The mutation operation refers to changing the value of some genes in an individual, that is, changing the binary value from 0 to 1 or from 1 to 0. After cross-over or mutation operations, a new generation of individuals is sent to the FDTD simulator for optimization. The entire optimization process is iterated for 150 generations, and the individual with the highest $I_{COVID-19}$ in the 150th generation is selected as the final optimized structure.

In the infrared band, the analyte's complex dielectric function contains the vibrational information of the molecular bond, which is essential for the early screening of metal structures. Therefore, to quickly optimize the metal layer structure with high detection ability, it is necessary to introduce the analyte's complex dielectric function into the FDTD. Figure 2b shows the infrared spectrum of COVID-19

https://doi.org/10.1021/acs.analchem.1c01078
Anal. Chem. 2021, 93, 9437−9444

virus particles.[11] Among them, the infrared absorption peaks A−E are selected as the typical fingerprint vibration peaks of COVID-19. The fingerprint vibration peaks of the new coronavirus and their respective tentative assignments are shown in Table S3. Subsequently, we used the Drude-Lorentz model[35] to fit the complex dielectric function of COVID-19 with the following expression

$$\varepsilon(\omega) = \varepsilon_\infty + \sum_{i=1}^{n} \frac{S_i}{(\omega_i^2 - \omega^2 - j\omega\gamma_i)} \quad (1)$$

where the high-frequency constant term, ε_∞ = 2.05; the oscillator resonance frequency, ω_1 = 1098.67 cm^{-1}, ω_2 = 1025.32 cm^{-1}, ω_3 = 975.71 cm^{-1}, ω_4 = 922.95 cm^{-1}, and ω_5 = 857.57 cm^{-1}; the oscillator strengths, S_1 = 46.74 cm^{-2}, S_2 = 136.98 cm^{-2}, S_3 = 179.70 cm^{-2}, S_4 = 125.76 cm^{-2}, and S_5 = 70.86 cm^{-2}; and the damping frequency, γ_1 = 16.38 cm^{-1}, γ_2 = 49.72 cm^{-1}, γ_3 = 38.84 cm^{-1}, γ_4 = 30.80 cm^{-1}, and γ_5 = 24.70 cm^{-1}. Figure 2c shows the real part (black curve) and imaginary part (red curve) of the COVID-19 complex dielectric function. To verify the fitting parameters' rationality, we imported the extracted complex dielectric function into the FDTD and simulated the absorption spectrum of COVID-19 with a thickness of 3 μm (Figure S4). It can be seen that the simulated spectrum of COVID-19 is in good agreement with the absorption spectrum measured by the experiment. In the FDTD simulation, we uniformly use the COVID-19 molecular layer with a thickness of 10 nm to optimize the metal structure

RESULTS AND DISCUSSION

Design and Simulation. Through the GA program and FDTD simulation, we obtained a metal structure with high detection ability. Figure 3a is a conceptual diagram of a single unit cell of a plasmonic biosensor. The sensor consists of two layers of MgF_2 that transmit infrared light and a layer of 100 nm (t_1)-thick periodic metal structure. The metal structure is prepared on the top MgF_2. A fluid channel separates the two layers of MgF_2 with a depth of 500 nm (t_2). The array period of the metal structure P = 3.5 μm and the width w = 0.7 μm. The plasmonic sensor is simulated using commercial software FDTD. In the simulation, we used periodic boundary conditions along the x-axis and y-axis and perfectly matched layer boundary conditions along the z-axis. The x-polarized light was incident perpendicularly along the negative direction of the z-axis. The transmission (T), reflection (R), and absorption spectra ($A = 1-T-R$) of the device are shown in Figure 3b. The transmission spectrum reaches its maximum at a wavelength of 8.5 μm; the transmission intensity is about 88%, and the full width at half maxima is 4.77 μm. In addition, the resonance peak of the transmission spectrum can be adjusted by changing the period. The corresponding unit cell model and simulation of the transmission spectrum are shown in Figure S5. Due to the metal structure's high symmetry, the transmission spectrum of the sensor exhibits polarization-independent characteristics (Figure 3c). This feature can avoid the use of polarizers in the test process while simplifying the test platform, which is more conducive to the application and promotion of plasmonic biosensors. Figure 3d shows the surface field intensity distribution of the metal structure at resonance. The local electric field is mainly concentrated at the tip of the pattern along the polarization direction, forming an electric dipole, which is consistent with the tip effect reported previously. When the analyte is distributed near the tip, the molecular vibrations of the analyte and the electric dipole of the plasmon resonance are strongly coupled. This coupling produces a SEIRA effect, thereby enhancing the intensity of the molecular vibration. The SEIRA from the metal structure makes the plasmonic sensor a good candidate for COVID-19 detection.

To further study the SEIRA capability of the plasmonic sensor, we simulated the transmission spectrum of a 10 nm-thick COVID-19 molecular layer when it was adsorbed on the surface of a metal structure in an air environment, as shown in Figure 3f. The solid black line and the solid blue line represent the transmission spectra before and after the metal structure adsorbs COVID-19 molecules, respectively. The red dashed line is the calibration baseline, and the light-orange shaded part is the infrared fingerprint vibration peak of COVID-19. When virus molecules cover the metal structure's surface, the transmission spectrum changes significantly (blue curve in Figure 3f). This change includes spectral redshift (the spectral redshift is related to the refractive index in the cavity) and linear changes. To quantify this linear change, we calculated the relative absorption spectrum of COVID-19, where $\Delta T = T_{fit} - T_{COVID\text{-}19}$, as shown in the magenta curve in Figure 3h. For comparison, the spectra of 10 nm-thick COVID-19 virus molecules and 450 nm-thick virus molecules covering MgF_2 are simulated, as shown in Figure 3h. No signal is observed when the 10 nm-thick COVID-19/MgF_2 (solid black line) is simulated. However, the signal of the 10 nm-thick COVID-19 molecules covering the metal structure is very obvious (solid magenta line). The signal strength of a 10 nm-thick COVID-19 molecules covering a metal structure is equivalent to that of a 450 nm-thick COVID-19/MgF_2 (solid red line), which is attributed to the SEIRA effect of the metal structure. The COVID-19 virus molecules are not only present in exhaled breath or droplets but also in nasopharyngeal swabs and saliva. It means that the use of plasmonic biosensors to detect the new coronavirus in a liquid environment is also critical. To this end, we simulated the transmission spectrum of the plasmonic metal structure in a liquid environment (Figure S6) and its ability to detect viruses in a liquid environment (Figure 3g). In the simulation, the liquid (H_2O) refractive index adopts Palik's built-in data and the liquid depth is 500 nm. The modeling diagrams are shown in Figure 3e. When the virus molecules are loaded onto the device, the liquid environment's redshift is much smaller than that in the gas environment. Because the refractive index of water is closer to the refractive index of virus molecules than air, therefore, in a liquid environment, the presence of virus molecules will not significantly change the refractive index in the nanofluidic channel, resulting in a smaller redshift. The plasmonic sensor's spectral response to viruses in a liquid environment is consistent with the spectral response to viruses in an air environment (Figure 3h), which implies that the proposed plasmonic sensor can be used for both liquid- and gas-detection environments. In addition, we also discussed the impact of spectral detuning on SEIRA signal strength from both simulation and theoretical aspects (see Supporting Information, Section S1 and Section S2 for details).

Quantitative Detection. The quantitative detection of the novel coronavirus is of extremely important significance in clinical medicine.[36] Quantitative detection of the virus before treatment can help doctors choose suitable drugs according to the virus level in clinical medicine. Quantitative detection of the virus during or after treatment can explore the effect of drugs on the virus and the effect of antiviral therapy. Therefore,

https://doi.org/10.1021/acs.analchem.1c01078
Anal. Chem. 2021, 93, 9437−9444

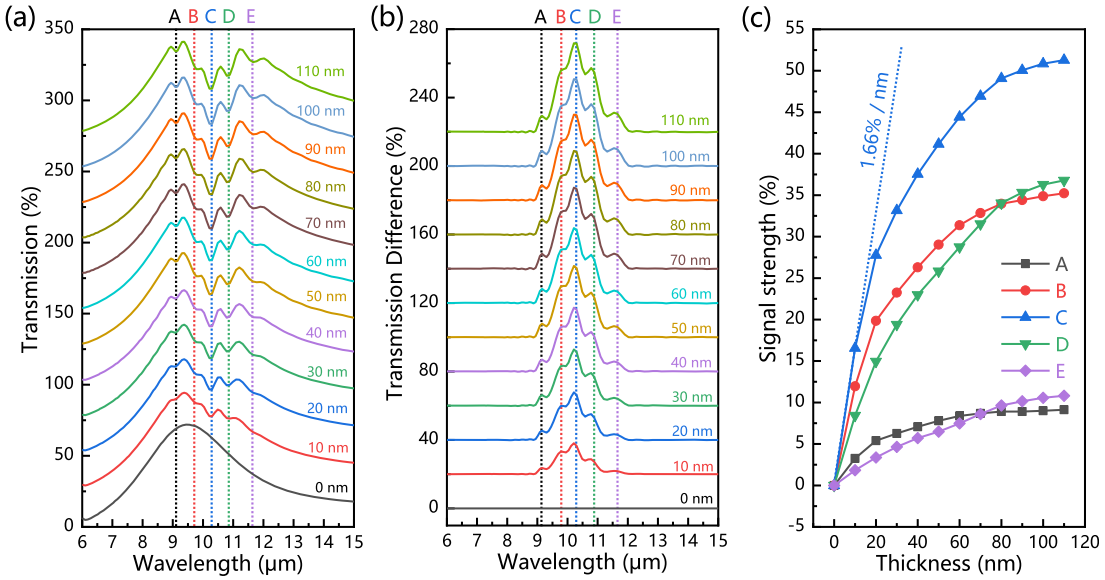

Figure 4. Thickness simulation of COVID-19 using the plasmonic biosensing platform in the liquid environment. (a) Transmission spectra of the metal structure covered with different thicknesses of the COVID-19 molecular layer. The thickness of the COVID-19 molecular layer varies from 0 to 110 nm. (b) Corresponding relative signal spectrum. (c) Relative signal strength of the five fingerprint peaks (A–E) of COVID-19 molecules varies with thickness.

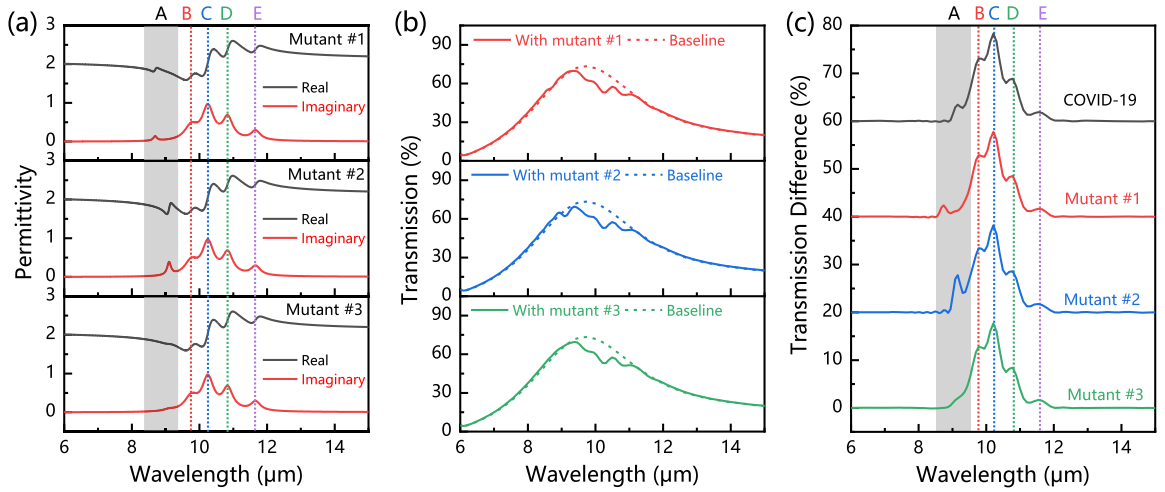

Figure 5. (a) Real (black) and imaginary (red) parts of the complex permittivity of three mutant COVID-19 molecules. (b) Simulated transmission spectra (solid line) of different mutant virus molecules coated with metal structure. The film thickness of the mutant virus molecules is unified to 10 nm. The dashed line is the calibration baseline of the corresponding transmission spectrum. (c) Relative signal spectrum of mutant COVID-19 molecules extracted from the transmission spectrum (b). The black curve in (c) refers to the relative signal spectrum of a 10 nm COVID-19 (original) molecular layer coated on the metal structure.

it is necessary to study the quantitative detection function of plasmonic sensors. In this part, we use plasmonic sensors to simulate different levels of virus molecules. To simplify the simulation model, we converted the level of COVID-19 content into the thickness of the COVID-19 molecular layer. Considering that the transmission spectrum of the metal structure will be red-shifted after covering the COVID-19 molecular layer, we chose the metal structure design of S2 (Section S5) and simulated the transmission spectrum with the thickness of the virus molecular layer from 0 to 110 nm in a liquid environment, as shown in Figure 4a. To study the proposed design's sensitivity, we calculated the metal structure's signal spectra at different viral molecular layer thicknesses from 0 to 110 nm (Figure 4b). Here, we observe five obvious vibration peaks (A–E), and the signal of vibration peak C is much larger than the signals of other peaks, which is related to their vibration intensity. To clearly understand the thickness-dependent sensitivity, we plotted the relationship between the signal intensity of each peak and the thickness of the viral molecular layer in Figure 4c. The results show that the signal intensity rises sharply as the thickness of COVID-19 layer increases and then saturates in the thicker layer, which is determined by the near-field distribution of the plasmonic device. To prove this hypothesis, we used FDTD simulation to calculate the spatial distribution of the near-field electric field strength along the direction perpendicular to the surface of the metal structure (Figure S7). The results show that the near-field intensity attenuates sharply as it moves away from the gold surface, and the attenuation value is 10% at 100 nm. Because the small spatial scale of the metal structure surface

https://doi.org/10.1021/acs.analchem.1c01078
Anal. Chem. 2021, 93, 9437–9444

contains a large field enhancement, our sensor is most sensitive when the molecular layer is thin, and the maximum sensitivity can reach 1.66%/nm. In addition, we also simulated the ability of the proposed plasmonic biosensor to detect COVID-19 in a gas environment quantitatively, and the simulation results are shown in Figure S8. The simulation results show that the proposed plasmonic biosensor also has a quantitative detection function in a gas environment. Thus, the plasmonic biosensor will become a good tool in the quantitative detection of novel coronaviruses.

Mutant Virus Screening. The novel coronavirus is prone to mutations because its genetic material (RNA) is a single-stranded structure. Some mutations can cause changes in the structure or configuration of the translated protein. These changes can be distinguished by Fourier transform infrared (FTIR) spectroscopy. Therefore, FTIR is expected to identify novel coronaviruses that have mutated by analyzing the fingerprint vibration peaks' changes. Here, we demonstrated through simulation that the plasmonic biosensor screens virus molecules with different fingerprint vibrations. Because the complex dielectric function of the molecule contains the information of the fingerprint vibration of the molecule, we can obtain a hypothetical mutant virus by modifying the complex dielectric function of COVID-19. According to eq 1, we know that each vibration peak is mainly affected by three parameters, which are the oscillator resonance frequency (w_i), the oscillator strengths (S_i), and the damping frequency (γ_i). To enhance the contrast, we only change the three parameters of the first vibration peak (A) while keeping other parameters unchanged. The newly obtained complex dielectric function is shown in Figure 5a (the specific parameter settings of the mutant virus are shown in Table S2). Next, we simulated the transmission spectrum of 10 nm-thick mutant virus molecules coated on the metal structure in a liquid environment (solid line in Figure 5b), and the dashed line in Figure 5b is the corresponding calibration baseline. Figure 5c extracted and plotted the absorption spectrum of the novel coronavirus and hypothetical mutant virus. Figure S9 shows the signal difference spectrum between the hypothetical mutant virus and the original virus. The hypothetical mutant virus can be easily distinguished by comparing the intensity and resonance frequency of peak A, which implies that the plasmonic infrared sensor is expected to play a unique role in detecting mutant viruses. In addition, the integration of manual intelligence and the infrared spectrum database can further realize the rapid analysis of viruses and the identification of mutated viruses.

CONCLUSIONS

In summary, we designed an ultra-sensitive and multi-functional plasmonic infrared sensor based on a GA intelligent program for the rapid detection of novel coronaviruses. The program starts with randomly generated patterns and then iteratively optimizes until the desired design goal is reached. Finally, a metal structure with ultra-high sensitivity and polarization-independence is optimized in the specific 6−15 μm band. We emphasize that the developed program can be easily extended to other metasurface designs. The optimized metal structure and nanofluidic channels are combined to construct an ultra-sensitive plasmonic infrared sensor. The sensor uses the characteristics of the infrared fingerprint vibration peak to achieve rapid detection of the novel coronavirus in a liquid or gas environment. We also theoretically studied the influence of spectral detuning on the enhancement of the analyte signal to guide the device's design. In addition to virus qualitative detection (determining negative or positive), the sensor we developed can also detect the virus quantitatively. The FDTD simulation results show that the maximum sensitivity of the sensor in a liquid environment can reach 1.66%/nm. The sensor's ultra-high sensitivity and infrared fingerprint-recognition characteristics also make it an ideal choice for mutant virus identification. In short, the plasmonic infrared sensor is expected to serve as a new virus pre-screening tool to allow early detection of infected persons and maximum control of new pandemics.

ASSOCIATED CONTENT

Supporting Information

The Supporting Information is available free of charge at https://pubs.acs.org/doi/10.1021/acs.analchem.1c01078.

GA program designing other structures; cross-over/mutation operator's idea and frequency spectrum simulation; simulation of the COVID-19 molecule's fingerprint vibration spectrum; dependence of resonance wavelength on structural parameters; spectral simulation in a liquid environment; near-field distribution of metal structure; quantitative detection of COVID-19 using a plasmonic biosensor in a gas environment; SEIRA spectral difference between a hypothetical mutant virus and the original virus; different effects of spectral detuning; temporal-coupled mode theory model; parameter setting of ω_a; parameter setting of the hypothetical mutant virus; and COVID-19 virus fingerprint vibration peaks and their assignments (PDF)

AUTHOR INFORMATION

Corresponding Authors

Xianming He − *Key Laboratory of Optoelectronic Technology & Systems of Ministry of Education, International R & D Center of Micro-nano Systems and New Materials Technology, College of Optoelectronic Engineering, Chongqing University, 400044 Chongqing, P. R. China*; Email: hexianming@cqu.edu.cn

Xiaojing Mu − *Key Laboratory of Optoelectronic Technology & Systems of Ministry of Education, International R & D Center of Micro-nano Systems and New Materials Technology, College of Optoelectronic Engineering, Chongqing University, 400044 Chongqing, P. R. China*; orcid.org/0000-0003-2024-2595; Email: mxjacj@cqu.edu.cn

Authors

Dongxiao Li − *Key Laboratory of Optoelectronic Technology & Systems of Ministry of Education, International R & D Center of Micro-nano Systems and New Materials Technology, College of Optoelectronic Engineering, Chongqing University, 400044 Chongqing, P. R. China*

Hong Zhou − *Key Laboratory of Optoelectronic Technology & Systems of Ministry of Education, International R & D Center of Micro-nano Systems and New Materials Technology, College of Optoelectronic Engineering, Chongqing University, 400044 Chongqing, P. R. China*; orcid.org/0000-0002-3146-2238

Xindan Hui − *Key Laboratory of Optoelectronic Technology & Systems of Ministry of Education, International R & D Center of Micro-nano Systems and New Materials*

https://doi.org/10.1021/acs.analchem.1c01078
Anal. Chem. 2021, 93, 9437−9444

Technology, College of Optoelectronic Engineering, Chongqing University, 400044 Chongqing, P. R. China

Complete contact information is available at: https://pubs.acs.org/10.1021/acs.analchem.1c01078

Author Contributions

All authors have given approval to the final version of the article.

Notes

The authors declare no competing financial interest.

■ ACKNOWLEDGMENTS

This work was supported by the National Natural Science Foundation of China (grant no. 52075061, 52005064), the National Key Research and Development Program of China (grant no. 2019YFB2004800), the China Postdoctoral Science Foundation (grant no. 2020M673129), and Fundamental Research Funds for the Central Universities (grant no. 2019CDCGGD320).

■ REFERENCES

(1) David, C. *Jama* **2020**, *323*, 2237−2238.
(2) Yao, H.; Song, Y.; Chen, Y.; Wu, N.; Xu, J.; Sun, C.; Zhang, J.; Weng, T.; Zhang, Z.; Wu, Z.; Cheng, L.; Shi, D.; Lu, X.; Lei, J.; Crispin, M.; Shi, Y.; Li, L.; Li, S. *Cell* **2020**, *183*, 730−738.
(3) Lan, J.; Ge, J.; Yu, J.; Shan, S.; Zhou, H.; Fan, S.; Zhang, Q.; Shi, X.; Wang, Q.; Zhang, L.; Wang, X. *Nature* **2020**, *581*, 215−220.
(4) Web Reference 1: COVID-19 Coronavirus Pandemic. https://www.worldometers.info/coronavirus/ (accessed 2021/03/01).
(5) Mercado, N.B.; et al. *Nature* **2020**, *586*, 583−588.
(6) Kim, J. H.; Marks, F.; Clemens, J. D. *Nat. Med.* **2021**, *27*, 205−211.
(7) Tanne, J. H. *Br. Med. J.* **2021**, *372*, n42.
(8) Jacqui, W. *Br. Med. J.* **2021**, *372*, n359.
(9) Kissler, S. M.; Tedijanto, C.; Goldstein, E.; Grad, Y. H.; Lipsitch, M. *Science* **2020**, *368*, 860−868.
(10) Vandenberg, O.; Martiny, D.; Rochas, O.; van Belkum, A.; Kozlakidis, Z. *Nat. Rev. Microbiol.* **2020**, *19*, 171−183.
(11) Valério, G. B.; Maneesh, N. S.; Leal, B. L.; Dantas, M. W.; Frizera, V. P.; Geraldo, M. J.; Rodrigo, R.-R.; Luciene, C. G. C.; Patrick, H. W.; Francis, L. M. *Anal. Chem.* **2021**, *93*, 2950−2958.
(12) Fang, Y.; Zhang, H.; Xie, J.; Lin, M.; Ying, L.; Pang, P.; Ji, W. *Radiology* **2020**, *296*, E115−E117.
(13) Bernheim, A.; Mei, X.; Huang, M.; Yang, Y.; Fayad, Z. A.; Zhang, N.; Diao, K.; Lin, B.; Zhu, X.; Li, K.; Li, S.; Shan, H.; Jacobi, A.; Chung, M. *Radiology* **2020**, *295*, 685−691.
(14) Long, Q.-X.; Tang, X.-J.; Shi, Q.-L.; Li, Q.; Deng, H.-J.; Yuan, J.; Hu, J.-L.; Xu, W.; Zhang, Y.; Lv, F.-J.; Su, K.; Zhang, F.; Gong, J.; Wu, B.; Liu, X.-M.; Li, J.-J.; Qiu, J.-F.; Chen, J.; Huang, A.-L. *Nat. Med.* **2020**, *26*, 1200−1204.
(15) Chen, Z.; Zhang, Z.; Zhai, X.; Li, Y.; Lin, L.; Zhao, H.; Bian, L.; Li, P.; Yu, L.; Wu, Y.; Lin, G. *Anal. Chem.* **2020**, *92*, 7226−7231.
(16) Long, Q. X.; et al. *Nat. Med.* **2020**, *26*, 845−848.
(17) Abbasi, J. *J. Am. Med. Assoc.* **2020**, *323*, 1881−1883.
(18) Smyrlaki, I.; Ekman, M.; Lentini, A.; Rufino de Sousa, N.; Papanicolaou, N.; Vondracek, M.; Aarum, J.; Safari, H.; Muradrasoli, S.; Rothfuchs, A. G.; Albert, J.; Högberg, B.; Reinius, B. *Nat. Commun.* **2020**, *11*, 4812.
(19) Udugama, B.; Kadhiresan, P.; Kozlowski, H. N.; Malekjahani, A.; Osborne, M.; Li, V. Y. C.; Chen, H.; Mubareka, S.; Gubbay, J. B.; Chan, W. C. W. *ACS Nano* **2020**, *14*, 3822−3835.
(20) Bai, Y.; Yao, L.; Wei, T.; Tian, F.; Jin, D.-Y.; Chen, L.; Wang, M. *J. Am. Med. Assoc.* **2020**, *323*, 1406−1407.
(21) Oran, D. P.; Topol, E. J. *Ann. Intern. Med.* **2020**, *173*, 362−367.
(22) Seo, G.; Lee, G.; Kim, M. J.; Baek, S. H.; Choi, M.; Ku, K. B.; Lee, C. S.; Jun, S.; Park, D.; Kim, H. G.; Kim, S. J.; Lee, J. O.; Kim, B. T.; Park, E. C.; Kim, S. I. *ACS Nano* **2020**, *14*, 5135−5142.
(23) Qiu, G.; Zhibo, G.; Yile, T.; Jean, S.; Gerd, A. K.-U.; Jing, W. *ACS Nano* **2020**, *14*, 5268−5277.
(24) Alafeef, M.; Ketan, D.; Parikshit, M.; Dipanjan, P. *ACS Nano* **2020**, *14*, 17028−17045.
(25) Neubrech, F.; Huck, C.; Weber, K.; Pucci, A.; Giessen, H. *Chem. Rev.* **2017**, *117*, 5110−5145.
(26) Mejía-Salazar, J. R.; Oliveira, O. N., Jr. *Chem. Rev.* **2018**, *118*, 10617−10625.
(27) Etezadi, D.; Warner, J. B.; Lashuel, H. A.; Altug, H. *ACS Sens.* **2018**, *3*, 1109−1117.
(28) Li, Z.; Zhu, Y.; Hao, Y.; Gao, M.; Lu, M.; Stein, A.; Park, A.-H. A.; Hone, J. C.; Lin, Q.; Yu, N. *ACS Photonics* **2019**, *6*, 501−509.
(29) Zhou, H.; Hui, X.; Li, D.; Hu, D.; Chen, X.; He, X.; Gao, L.; Huang, H.; Lee, C.; Mu, X. *Adv. Sci.* **2020**, *7*, 2001173.
(30) Hu, H.; Yang, X.; Guo, X.; Khaliji, K.; Biswas, S. R.; de Abajo, F. J. G.; Sun, Z.; Dai, Q.; Dai, Q. *Nat. Commun.* **2019**, *10*, 1131.
(31) Chen, S.; Liu, C.; Liu, Y.; Liu, Q.; Lu, M.; Bi, S.; Jing, Z.; Yu, Q.; Peng, W. *Adv. Sci.* **2020**, *7*, 2000763.
(32) Semenyshyn, R.; Hentschel, M.; Stanglmair, C.; Teutsch, T.; Tarin, C.; Pacholski, C.; Giessen, H.; Neubrech, F. *Nano Lett.* **2019**, *19*, 1−7.
(33) Ma, W.; Liu, Z.; Kudyshev, Z. A.; Boltasseva, A.; Cai, W.; Liu, Y. *Nat. Photonics* **2020**, *15*, 77−90.
(34) Kudyshev, Z. A.; Kildishev, A. V.; Shalaev, V. M.; Boltasseva, A. *Appl. Phys. Rev.* **2020**, *7*, 021407.
(35) Kuzmenko, A. B. *Rev. Sci. Instrum.* **2005**, *76*, 083108.
(36) Wölfel, R.; Corman, V. M.; Guggemos, W.; Seilmaier, M.; Zange, S.; Müller, M. A.; Niemeyer, D.; Jones, T. C.; Vollmar, P.; Rothe, C.; Hoelscher, M.; Bleicker, T.; Brünink, S.; Schneider, J.; Ehmann, R.; Zwirglmaier, K.; Drosten, C.; Wendtner, C. *Nature* **2020**, *581*, 465−469.